Scripta Materialia 162 (2019) 112–117

Contents lists available at ScienceDirect

Scripta Materialia

journal homepage: www.elsevier.com/locate/scriptamat

Superelastic effect in Ti-rich high entropy alloys *via* stress-induced martensitic transformation

Lu Wang, Chao Fu, Yidong Wu, Runguang Li, Xidong Hui *, Yandong Wang *

State Key Laboratory for Advanced Metals and Materials, University of Science and Technology Beijing, Beijing 100083, PR China

ARTICLE INFO

Article history:
Received 17 October 2018
Received in revised form 24 October 2018
Accepted 25 October 2018
Available online xxxx

Keywords:
High entropy alloys
Stress-induced martensitic transformation
Superelastic effect
In situ X-ray diffraction

ABSTRACT

This letter reports an outstanding superelastic effect in Ti-rich TiZrHfAlNb high entropy alloys for the first time, which is exhibited by comprehensive combination of the maximum total recovery strain, fully recoverable strain and corresponding tensile strength up to 5.2%, 4.0% and 900 MPa, respectively. It has been confirmed that these alloys are only composed of metastable β and martensite α″ phase, and ω phase is suppressed. The *in situ* X-ray diffraction experiment reveals that reversible stress-induced martensitic transformation between β ↔ α″ endows the alloys superelasticity, while the plastic deformation and reorientation of martensite inhibit the recovery phase transformation.

Stress-induced transformation, including stress-induced martensitic transformation (SIMT) and mechanical twinning, have been exploited as an important way to promote the plastic deformation capability of traditional steels, copper and titanium alloys [1]. Recently, the SIMT has been successfully used in strengthening of the high entropy alloys (HEAs), which are designed based on the concept of equimolar or near-equimolar components so that the alloys have high configuration entropy [2–4]. It has been shown that the combination of strength and ductility can be achieved by "metastability-engineering" strategy including transformation induced plasticity (TRIP) and twinning induced plasticity (TWIP) in both FCC and BCC HEAs, such as FeCoCrNiMn [5], Fe80-*x*Mn*x*Co10Cr10 [6], Ti35Zr27.5Hf27.5Nb5Ta5 [7], and TiZrNbHfTa*x* [8]. G. S. Firstov et al. [9] combined the high temperature shape memory alloys with HEAs for the first time. Considering that SIMT is the basic principle of shape memory and superelastic effects of metallic materials, whether it is possible to employ SIMT to acquire superelasticity in HEAs is still an open question. The key point for this purpose is that the phase stability of HEAs should be reduced and reversible phase transformation should take place during the loading-unloading process. In the present study, we report our finding of Ti-rich Ti50Zr20Hf15Al10Nb5 and Ti49Zr20Hf15Al10Nb6 HEAs with outstanding superelasticity due to reversible SIMT for the first time. To clarify the intrinsic origin of the superelasticity, the phase evolution and lattice strains for different planes of the composited phases as a function of tensile strain are investigated by *in situ* synchrotron high-energy X-ray diffraction. This work sheds light on the deformation mechanism and development of HEAs with new functional properties.

The alloys with nominal compositions of Ti50Zr20Hf15Al10Nb5 and Ti49Zr20Hf15Al10Nb6 (at%) were prepared by arc melting and drop-casting into water-cooled mold with sized of 10 × 10 × 45 mm^3. After homogenized, the alloy was cold rolled with 40% reduction in thickness. The DSC curves of the cold rolled samples are shown in Fig. 1(a), it can be seen that an endothermic peak appeared on the heating process from 674 °C to 771 °C for Nb5 and 642 °C to 746 °C for Nb6, which means that the recrystallization takes place during this period. Based on this peak temperature, the subsequent annealing treatment technologies was determined to be 0.5 h@800 °C and 0.5 h@900 °C, respectively, followed by quenching into water (hereafter the alloys are referred as Nb5-800, Nb5-900, Nb6-800 and Nb6-900 for convenience).

The room temperature tensile properties were tested using CMT4105 universal electronic tensile testing machine at a strain rate of 1 × 10^{-3} s^{-1} on dog-bone-shaped specimen with the gauge part of 20 × 3 × 1.7 mm^3. The phase composition of the interested alloys was tested using X-ray diffraction (XRD) with CuKα radiation (Rigaku Kmax 2500 V) in a scanning 2θ range of 20°–100° at a rate of 10° min^{-1}. The samples for optical microscopy (OM) were mechanically polished and etched at room temperature in a solution of HF, HNO_3 and H_2O. Further microstructural investigation was conducted by a Tecnai G2 F20 200 kV transmission electron microscope (TEM). TEM specimens were prepared from punched out 3 mm disks which were ground to about 60 μm, followed by twin-jet electro-polishing using a mixed solution of glacial acetic acid: perchloric acid: ethanol = 4:8:88 (in volume). The micro-deformation behavior was investigated using *in situ* synchrotron high-energy X-ray diffraction (HE-XRD) technique. The experiments were performed at the 11-1D-C beam line at the Advanced Photon Source, Argonne National Laboratory, USA. A monochromatic X-ray beam with wavelength of 0.11748 Å was used to study the

* Corresponding authors.
E-mail addresses: xdhui@ustb.edu.cn (X. Hui), ydwang@ustb.edu.cn (Y. Wang).

https://doi.org/10.1016/j.scriptamat.2018.10.035
1359-6462/

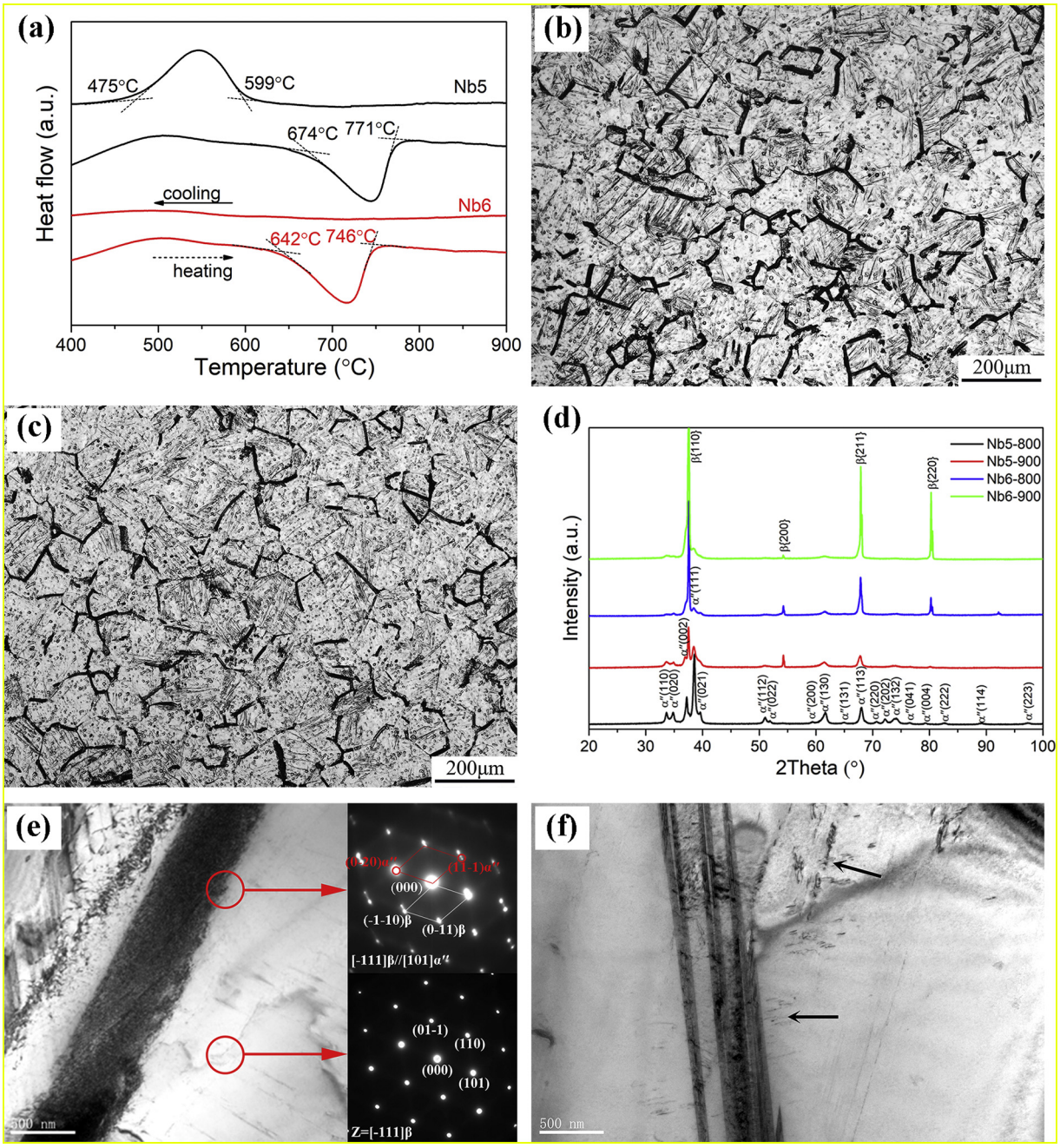

Fig. 1. (a) The DSC curves for the cold rolled Ti50Zr20Hf15Al10Nb5 and Ti49Zr20Hf15Al10Nb6 alloy; the OM photographs of Nb5-800 (b) and Nb5-900(c); (d) the XRD patterns of Nb5 and Nb6 alloys after thermo-mechanical treatment; the TEM photographs and SADPs of Nb5-800 (e) and Nb5-900(f).

structure evolution and change in lattice strain under tensile loading mode. The experimental set-up and the size of specimen are schematically illustrated in [10].

First, the microstructure and phase composition were characterized. The OM photographs of Nb5-800 and Nb5-900 alloys are shown in Fig. 1 (b) and (c). These two alloys contain equiaxed grains with flat and straight boundary, the grain size change from about 10 μm to 100 μm. There are lots of lath-shape second phase inside grains with different sizes. Fig. 1(d) shows the XRD patterns of the Nb5 and Nb6 alloys annealed at different temperatures. These alloys are composed of an orthorhombic α″-martensitic phase and a bcc β-parent phase. On the DSC curve of the cold rolled samples shown in Fig. 1(a), an exothermic peak appeared from 599 °C to 475 °C during the cooling process for Nb5, but no obvious peak for Nb6. These results mean that the α″ phase precipitated during cooling in Nb5. From Fig. 1(d), it is seen that the peaks of α″ phase are more apparent in Nb5 than those in Nb6 alloy and more apparent in the alloys with higher heat treatment temperature. That is to say, more metastable β phase survives when annealed at a higher temperature in the HEA with higher content of Nb since Nb is a β stabilizer. Besides, it is also noticeable that all the XRD patterns does not indicate the peaks of the athermal ω phase, which usually exists in Ti-Nb [11] and Ti-Ta [12] alloys and has pernicious effects on the shape memory or superelastic effect. It has been reported that in Ti-Zr-Nb-Al [13], Ti-Ta-Al [14] and Ti-V-Al [15] alloys, the formation of ω phase are also suppressed. Thus, the reason for the suppression of ω phase in these HEAs should be attributed to the addition of Al. And the suppression of ω phase and existence of metastable β phase should be beneficial to the phase transformation when stress is applied to these alloys. The lattice parameters of α″ in Nb5 are $a = 0.311$ nm, $b = 0.516$ nm, $c = 0.483$ nm, resulting in the b/a and c/a of 1.66 and 1.55. Both ratios are

higher than these of Ti-20Zr-10Nb alloy (1.631 and 1.535), meaning that lattice distortion increases with Hf and Al addition and decrease of Nb content. The lattice parameter of β phase in Nb5 is 0.339 nm. And the lattice parameters of α″ phase in Nb6 are $a = 0.312$ nm, $b = 0.514$ nm, $c = 0.490$ nm, and that of β phase in Nb6 is 0.338 nm. The TEM images and the corresponding selected area electron diffraction patterns (SADPs) of the Nb5 alloys are shown in Fig. 1(d) and (f). Both the β and α″ phases can be observed in the bright field images. The difference between the two alloys is that the α″ plates in Nb5-800 are broader than those in Nb5-900. And both alloys have lots of dislocations bands and loops in the β matrix which are induced by the thermo-mechanical treatment. The SADPs show an orientation relationship of $[-111]\beta // [101]\alpha''$, which is common in the titanium with superelastic and shape memory effect [16].

The tensile stress-stain curves of the two alloys, loading-unloading curves of Nb5 and cycle loading-unloading curves of Nb6 at room temperature are shown in Fig. 2. It is found that both alloys exhibit two-stage yielding behavior during tensile testing. The first yielding event occurred at about 0.4% strain at the critical stress (σ_{SIM} shown in Fig. 2 (b)) about 350 MPa for Nb5 and 480 MPa for Nb6. After the first

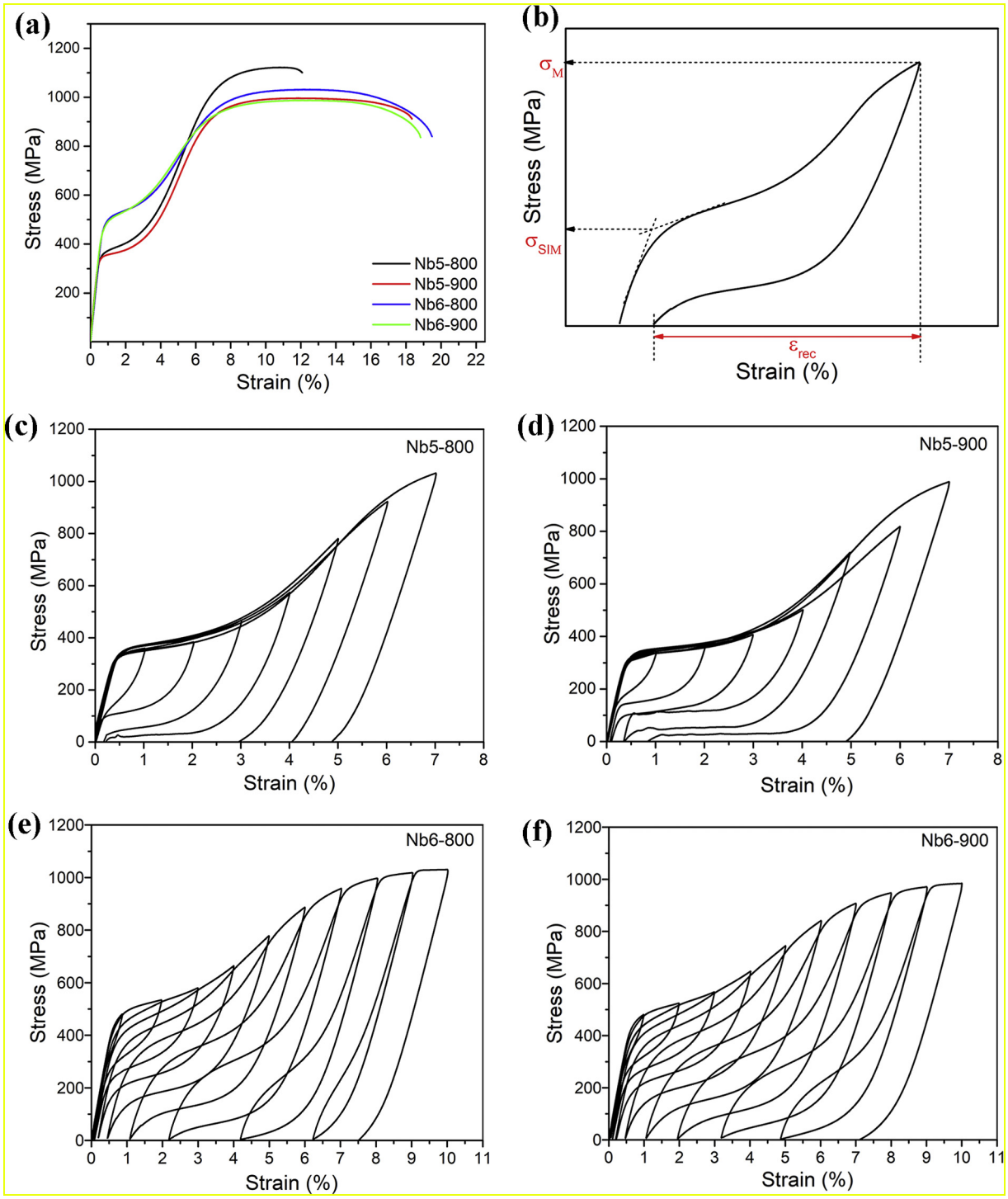

Fig. 2. The tensile stress-stain curves of Nb5 and Nb6 alloys (a), loading-unloading curves of Nb5-800(c), Nb5-900 (d) and cycle loading-unloading curves of Nb6-800 (e), Nb6-900 (f) at room temperature; (b) the superelastic properties determined by the cycle loading-unloading test including the maximum recovery strain (ε_{rec}) and the tensile strength (σ_M).

yielding, there is a stress plateau, and then the second work hardening stage is up to 8% strain followed by the second strain-stress plateau until fracture. The fracture strengths and elongations are 1066 MPa, 13% for Nb5-800, 996 MPa, 18% for Nb5-900, 1030 MPa, 19% for Nb6-800 and 987 MPa, 18% for Nb8-900, respectively. The loading-unloading curves obtained at some tensile strains show that the deformation almost recovered after unloading at 4% strain for Nb5-800 and 6% for Nb5-900. These results indicate that these HEAs exhibit superelasticity. Compared with Nb5, Nb6 alloy shows better superelasticity. The superelastic properties determined by the cycle loading-unloading test including the maximum recovery strain (ε_{rec}) and the tensile strength (σ_M) are defined in Fig. 2(b). Apparently, the superelasticity of Nb6-900 is better than that of Nb6-800. The maximum total recovery strain of Nb6-900 is about 5.2% and the σ_M is up to 900 MPa. When compared with the previous results on Ti-Nb(Mo), Ti-Nb-(Mo, Zr, Sn, Al) alloys [17–31] as shown in Fig. 3, the HEA alloys show excellent combination of superelasticity and high strength. And it is clear that present Nb6 alloy has the largest fully recoverable strain up to 4%, together with its high value of critical stress about 480 MPa, this material displays a great potential for biomedical applications. For example, for the dental appliances, the material for orthodontic wires requires appropriate superelasticity to adapt the applied strain and provide efficient correction stress upon strain recovery process.

Previous research [2] has shown that the presence of "stress plateau" is mainly caused by the extensive SIMT from $\beta \rightarrow \alpha''$ and/or α'' martensite variants reorientation occurring within a narrow stress/strain range, and the superelastic effect is due to the reversible martensitic transformation, namely $\beta \leftrightarrow \alpha''$. To clarify the mechanism of superelasticity of this HEA, *in situ* X-ray diffraction was performed for Nb5-800 during uniaxial tensile testing. Fig. 4(a) shows a part of straightened Debye-Scherrer diffraction rings of Nb5-800 alloy as a function of macroscopic strain. The diffraction intensity of $\{110\}\beta$ decreases and the intensity of $(110)\alpha''$, $(020)\alpha''$, $(111)\alpha''$, $(021)\alpha''$ peaks become stronger gradually with the increase of applied strain, implying that a progressive SIMT takes place. While as the strain goes up, the distribution of intensity of diffraction rings becomes more and more non-uniform. Specifically, the $(020)\alpha''$ and $(021)\alpha''$ tend to distribute in the loading direction (*i.e.*, a 10° azimuthal bin around 90° and 270°), and $(110)\alpha''$, $(002)\alpha''$ and $(111)\alpha''$ tend to distribute in the Poisson direction (*i.e.*, a 10° azimuthal bin around 0° and 180°). The texture produced during loading implies the reorientation of α'' during the later deformation. This is in good accordance with the previously published results that SIMT and reorientation of martensite variants are strongly dependent on the crystallographic orientation with respect to the external stress [32]. The texture developed by the combined SIMT and martensite variants reorientation is explained in the Ti-33Nb-4Sn alloy which is also composed of metastable β and α'' [33,34]. When the initial α'' formed during quenching is subjected to the applied stress, the SIMT occurs with the $[002]\alpha''$ direction being aligned to tensile direction, and $[100]\alpha''$ and $[002]\alpha''$ being perpendicular to tensile direction, which could accommodate the macroscopic strain to the greatest extent [16].

To characterize the volume fraction of β and α'' phase more clearly, the intensity of whole Debye-Scherrer diffraction ring were integrated as shown in Fig. 4(b). It can be seen that the relative integrated intensity of $\{110\}\beta$ decreases slightly before 0.4%, decreased at a higher rate within the strain range from 0.4% to 4%, and decreased at a lower rate up to 7%. The $\{002\}\beta$ are in the same situation, except that the $\{002\}\beta$ increased firstly and then decreased before 0.4%, indicating the existence of tiny sample rotation during the elastic deformation. Meanwhile, the relative integrated intensity of $(002)\alpha''$ increases at about 0.5%, increases intensely in 0.5% to 1.0% strain, and increases relatively slowly during the range from 1.0% to 5.5%. When the strain is beyond 5.5%, the intensity of $(002)\alpha''$ decreases until 7.2%. Above that strain, the intensity increases again. This further suggests that the reorientation of α'' occurred during tensile straining. The intensity of $(110)\alpha''$ increases drastically from 0.4% to 1%, and almost keeps the same from 1.0% to 4.0%, and then increases slowly above 4.0%. The reduction of β phase and increase of α'' suggests that SIMT continues during the whole tensile before facture, while reorientation of α'' takes place at 4.0%.

The deformation mechanism of the HEA could further be understood from the evolution of the lattice strain. The lattice strains for the different planes of β and α'' phases as a function of microscopic strain in the tensile direction are shown in Fig. 4(c). Being consistent with the tensile stress-strain curves, the curves of lattice strain *versus* tensile stress can also be divided into four stages under different stresses. When the strain is less than 0.4%, all the planes of β and α'' phases respond linearly to the stress, which implies that the alloy suffered elastic deformation during this period. The difference of the slopes among different peaks is due to the crystallographic orientation and elastic stiffness. As the strain

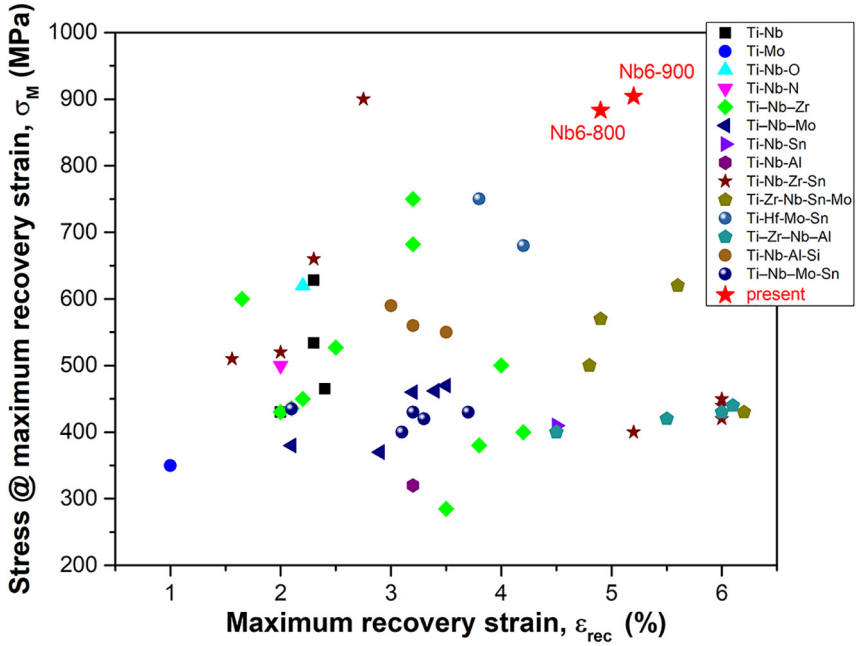

Fig. 3. The comparison map of maximum recovery strain and the corresponding stress including various Ni free Ti-based superelastic alloys and the present HEAs.

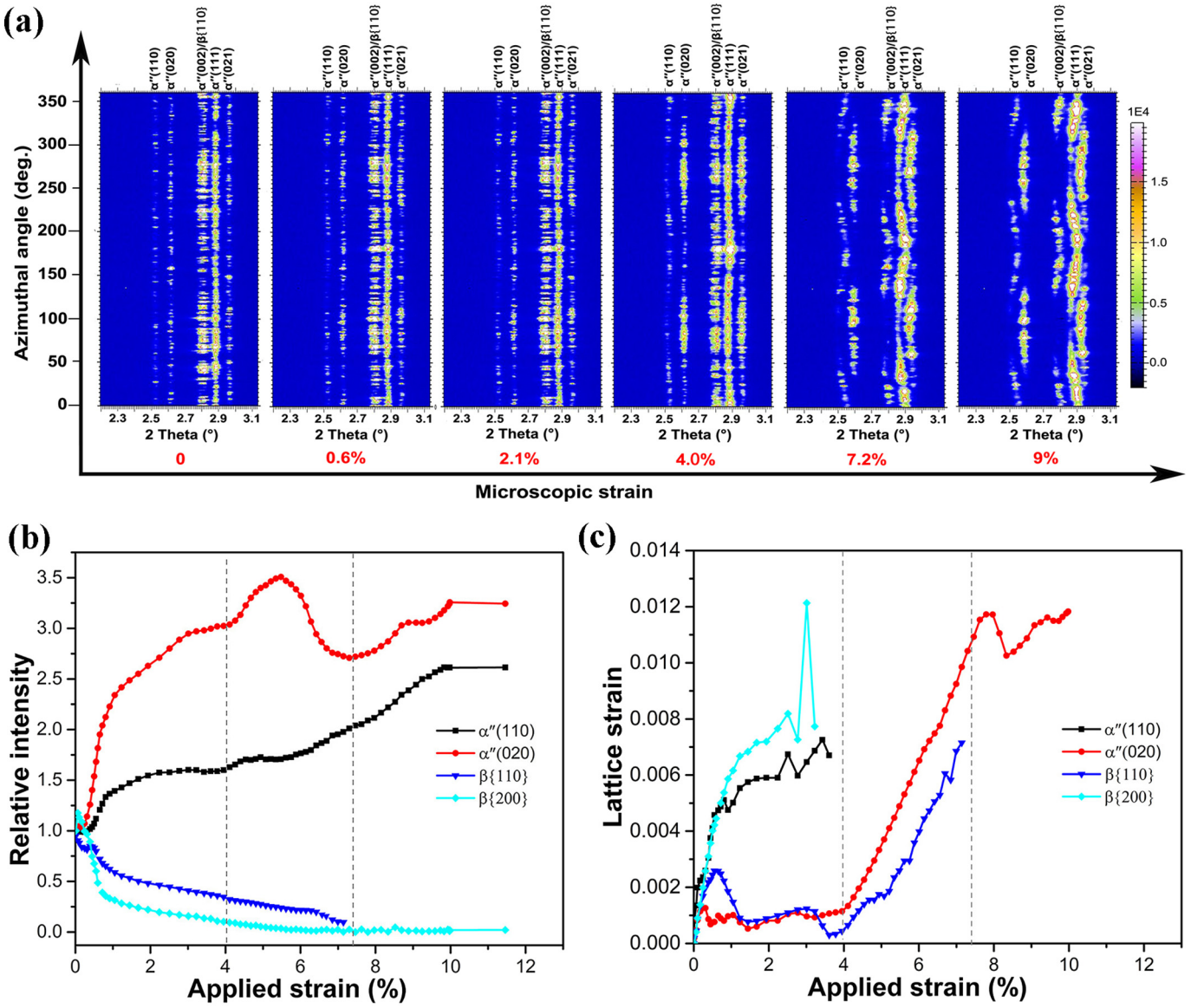

Fig. 4. The *in situ* X-ray diffraction results of the Nb5-800 alloy. (a) Parts of the straightened Debye-Scherrer diffraction rings as a function of macroscopic strain; (b) the integrated intensity of the whole Debye-Scherrer diffraction ring as a function of applied strain; (c) lattice strain along the loading direction as a function of applied strain.

surpasses 0.4%, elastic deformation of β and α″ phases breaks down, and the SIMT starts. In the stage II (0.4% to 4.0%), the slope of (110)α″ is almost equal to zero, that is to say, there is a lattice strain platform at which the lattice strain keep constant even though it was applied strain. This is related to the fact that the ongoing SIMT accommodates the macroscopic strain. When the strain is above 4.0%, only (020)α″ and small amount of {110}β can be detected in the loading direction. The tensile stress-strain curves increase with a certain slope and the lattice strain of (020)α″ responds linearly to the tensile stress, but the slope is smaller than that before 0.4% strain, demonstrating that the elastic deformation of α″ phase is companied with small amount of reorientation of α″. When the strain is greater than 7.2% (stage IV), the lattice strain and the applied stress decrease simultaneously, meaning that the second yielding takes place. After that, the fracture occurs for the HEA. So, the four stages during tensile deformation can be classified as: 1) the elastic deformation of the quenching formed α″ and metastable β; 2) SIMT activated at 0.4% and processing intensely to 4% strain, 3) pseudoelastic deformation of the initial α″, the new-born α″ and the residual β phase accompanied by the reorientation of α″ and small amount of SIMT; 4) the plastic deformation of the alloy.

As can be seen, SIMT from β to α″ and the reorientation of α″ occur during loading in the Nb5-800 alloy. The SIMT taking place drastically during 0.4% to 4.0% strain is reversible. Thus, the sample shows almost complete strain recovery before 4.0%. And after that, the pseudoelastic deformation of the composed phase and reorientation of α″ become predominant, so that the superelasticity disappears. Compared with Nb5-800 alloy, the SIMT in Nb5-900, Nb6-800 and Nb6-900 alloys will maintain high level in large deformation due to the more β phase. According to the calculation in [16], the maximum transformation strain ε_M along the [011]β direction is 7.5% for Nb5 alloy and 7.36% for Nb6 alloy, which are larger than that of the traditional Ti-based shape memory alloys. This endows the HEAs with large shape recovery strain. On the other hand, highly solid solution strengthening ensures the high critical stress for the SIMT.

In conclusion, the Ti-rich Ti50Zr20Hf15Al10Nb5 and Ti49Zr20Hf15Al10Nb6 high entropy alloys exhibit outstanding superelastic strains. In the thermo-mechanical treated alloy, metastable β and α″ phase coexist. The *in situ* X-ray diffraction study of Nb5-800 under uniaxial tensile reveals that the reversible SIMT between β ↔ α″ endows the alloy superelasticity during unloading. Beyond that, the plastic deformation and reorientation of martensite suppress the

recovery. It is expected that the finding of superelastic effect in this Ti-Zr-Hf-Al-Nb system will trigger new applications of the high entropy alloys in the fields of aerospace engineering and biomedical applications.

Acknowledgments

This work was financially supported by The National Key Basic Research Program (2016YFB0701402), National Natural Science Foundation of China (Nos. 51571016 and 51771020), Key Laboratory of Research on Hydraulic and Hydro-Power Equipment Surface Engineering Technology of Zhejiang Province (2017SLKL003). The use of the Advanced Photon Source was supported by the US Department of Energy, Office of Science, Office of Basic Energy Sciences, under Contract No. DE-AC02-06CH11357.

References

[1] K. Yamauchi, I. Ohkata, K. Tsuchiya, S. Miyazaki (Eds.), Shape Memory and Superelastic Alloys: Applications and Technologies, Elsevier, 2011.
[2] Y. Zhang, T.T. Zuo, Z. Tang, M.C. Gao, K.A. Dahmen, P.K. Liaw, Z.P. Lu, Prog. Mater. Sci. 61 (2014) 1–93.
[3] Y.F. Ye, Q. Wang, J. Lu, C.T. Liu, Y. Yang, Mater. Today 19 (2016) 349–362.
[4] O.N. Senkov, G.B. Wilks, D.B. Miracle, C.P. Chuang, P.K. Liaw, Intermetallics 18 (2010) 1758–1765.
[5] B. Gludovatz, A. Hohenwarter, D. Catoor, E.H. Chang, E.P. George, R.O. Ritchie, Science 345 (2014) 1153–1158.
[6] Z. Li, K.G. Pradeep, Y. Deng, D. Raabe, C.C. Tasan, Nature 534 (2016) 227–231.
[7] L. Lilensten, J.P. Couzinié, J. Bourgon, L. Perrière, G. Dirras, F. Prima, I. Guillot, Mater. Res. Lett. (2016) 1–7.
[8] H. Huang, Y. Wu, J. He, H. Wang, X. Liu, K. An, W. Wu, Z. Lu, Adv. Mater. 29 (2017) 1701678.
[9] G.S. Firstov, T.A. Kosorukova, Y.N. Koval, et al., Shap. Mem. Superelasticity 1 (4) (2015) 400–407.
[10] L. Ma, L. Wang, Z. Nie, F. Wang, Y. Xue, J. Zhou, T. Cao, Y. Wang, Y. Ren, Acta Mater. 128 (2017) 12–21.
[11] Y. Al-Zain, H.Y. Kim, H. Hosoda, et al., Acta Mater. 58 (12) (2010) 4212–4223.
[12] P.J.S. Buenconsejo, H.Y. Kim, H. Hosoda, et al., Acta Mater. 57 (4) (2009) 1068–1077.
[13] F. Zhang, Z.G. Yu, C.Y. Xiong, W.T. Qu, B.F. Yuan, Z.G. Wang, Y. Li, Mater. Sci. Eng. A 679 (2017) 14–19.
[14] P.J.S. Buenconsejo, H.Y. Kim, S. Miyazaki, Scr. Mater. 64 (2011) 1114–1117.
[15] Z.Y. Yang, X.H. Zheng, W. Cai, Scr. Mater. 99 (2015) 97–100.
[16] H.Y. Kim, Y. Ikehara, J.I. Kim, H. Hosoda, S. Miyazaki, Acta Mater. 54 (2006) 2419–2429.
[17] C. Wang, M. Liu, P. Hu, J. Peng, J. Wang, Z. Ren, G. Cao, J. Alloys Compd. 720 (2017) 488–496.
[18] E. Takahashi, T. Sakurai, S. Watanabe, N. Masahashi, S. Hanada, Mater. Trans. 43 (12) (2002) 2978–2983.
[19] Y. Hao, S. Li, S. Sun, C. Zheng, R. Yang, Acta Biomater. 3 (2) (2007) 277–286.
[20] Y. Yang, P. Castany, M. Cornen, F. Prima, S. Li, Y. Hao, T. Gloriant, Acta Mater. 88 (2015) 25–33.
[21] Z.X. Hang, S.J. He, Z. Xin, Y.Z. Yi, C. Wei, Chin. Phys. B 23 (1) (2013), 018101. .
[22] A. Ramarolahy, P. Castany, F. Prima, P. Laheurte, I. Péron, T. Glorian, J. Mech. Behav. Biomed. 9 (2012) 83–90.
[23] F. Sun, Y. Hao, S. Nowak, T. Gloriant, P. Laheurte, F. Prima, J. Mech. Behav. Biomed. 4 (8) (2011) 1864–1872.
[24] J.I. Kim, H.Y. Kim, T. Inamura, H. Hosoda, S. Miyazaki, Mater. Trans. 47 (3) (2006) 505–512.
[25] K. Masumoto, Y. Horiuchi, T. Inamura, H. Hosoda, K. Wakashima, H. Kim, S. Miyazaki, Mater. Sci. Eng. A 438 (2006) 835–838.
[26] M.F. Ijaz, H.Y. Kim, H. Hosoda, S. Miyazaki, Scr. Mater. 72 (2014) 29–32.
[27] Y. Hao, S. Li, S. Sun, R. Yang, Mater. Sci. Eng. A 441 (1–2) (2006) 112–118.
[28] F. Sun, S. Nowak, T. Gloriant, P. Laheurte, A. Eberhardt, F. Prima, Scr. Mater. 63 (11) (2010) 1053–1056.
[29] J. Zhang, F. Sun, Y. Hao, N. Gozdecki, E. Lebrun, P. Vermaut, R. Portier, T. Gloriant, P. Laheurte, F. Prima, Mater. Sci. Eng. A 563 (2013) 78–85.
[30] Y. Fukui, T. Inamura, H. Hosoda, K. Wakashima, S. Miyazaki, Mater. Trans. 45 (4) (2004) 1077–1082.
[31] E. Bertrand, T. Gloriant, D. Gordin, E. Vasilescu, P. Drob, C. Vasilescu, S. Drob, J. Mech. Behav. Biomed. 3 (8) (2010) 559–564.
[32] S.L. Raghunathan, M.A. Azeem, D. Collins, D. Dye, Scr. Mater. 59 (2008) 1059–1062.
[33] S. Guo, Y. Shang, J.S. Zhang, Q.K. Meng, X.N. Cheng, X.Q. Zhao, Mater. Sci. Eng. A 692 (2017) 81–89.
[34] S. Guo, Y. Shang, J.S. Zhang, Q.K. Meng, X.N. Cheng, X.Q. Zhao, Intermetallics 86 (2017) 20–24.